MNRAS **000**, 1–16 (2016) Preprint 26 April 2016 Compiled using MNRAS LATEX style file v3.0

Morphology and kinematics of the gas envelope of Mira Ceti

P. T. Nhung*, D. T. Hoai, P. N. Diep, N. T. Phuong, N. T. Thao, P. Tuan-Anh and P. Darriulat

Department of Astrophysics, Vietnam National Satellite Center, VAST, 18 Hoang Quoc Viet, Hanoi, Vietnam

arXiv:1603.00148v2 [astro-ph.SR] 25 Apr 2016

Accepted XXX. Received YYY; in original form ZZZ

ABSTRACT

Observations of ^{12}CO(3-2) emission of the circumbinary envelope of Mira Ceti, made by ALMA are analysed. The observed Doppler velocity distribution is made of three components: a blue-shifted south-eastern arc, which can be described as a ring in slow radial expansion, ∼1.7 km s^{-1}, making an angle of ∼50° with the plane of the sky and born some 2000 years ago; a few arcs, probably born at the same epoch as the blue-shifted arc, all sharing Doppler velocities red-shifted by approximately 3±2 km s^{-1} with respect to the main star; the third, central region dominated by the circumbinary envelope, displaying two outflows in the south-western and north-eastern hemispheres. At short distances from the star, up to ∼1.5″, these hemispheres display very different morphologies: the south-western outflow covers a broad solid angle, expands radially at a rate between 5 and 10 km s^{-1} and is slightly red shifted; the north-eastern outflow consists of two arms, both blue-shifted, bracketing a broad dark region where emission is suppressed. At distances between ∼1.5″ and ∼2.5″ the asymmetry between the two hemispheres is significantly smaller and detached arcs, particularly spectacular in the north-eastern hemisphere are present. Close to the stars, we observe a mass of gas surrounding Mira B, with a size of a few tens of AU, and having Doppler velocities with respect to Mira B reaching ±1.5 km s^{-1}, which we interpret as gas flowing from Mira A toward Mira B.

Key words: stars: AGB and post-AGB – circumstellar matter – stars: individual: Mira AB – radio lines: stars.

1 INTRODUCTION

Mira Ceti is one of the most studied binary stars. Its distance from the Sun is estimated to be 107±10 pc from the Hipparcos catalogue and 91.7 pc by van Leeuwen (2007). In the present work we retain a distance of 100 pc, meaning that an angular distance projected on the sky of 1″ corresponds to 100 AU and is covered in ∼500 yr at a projected velocity of 1 km s^{-1}. The infrared environment has been recently observed over ∼ 5′ using Herschel PACS by Mayer et al. (2011) at 70 and 160 μm.

The main star, Mira A, is a long period variable that has been on the Asymptotic Giant Branch (AGB) long enough to display technetium in its spectrum (Little et al. 1987; Kipper 1992). It is an M.7 type, oxygen-rich star with a mass loss rate of the order of 10^{-7} M$_\odot$ yr^{-1}(Mauron & Caux 1992; Knapp et al. 1998; Ryde & Schöier 2001). It has a mass of 1.2 solar masses (Wyatt & Cahn 1983), a luminosity of ∼9000 solar luminosities and a temperature of ∼3000 K (Woodruff et al. 2004). Its apparent magnitude varies between as low as ∼2 and as high as ∼10 with a pulsation period of 333 days (Templeton & Karovska 2009). It has a very high velocity with respect to the local ISM, of the order of 120 km s^{-1}, oriented approximately from north to south (van Leeuwen 2007). A bow shock is visible in front of Mira A at a distance of ∼3′ from it (Martin et al. 2007). It generates a cometary wake visible over ∼2° that has been observed in the UV (Martin et al. 2007) and the interaction of the circumstellar envelope with the interstellar medium has been seen in HI (Matthews et al. 2008). Evidence for the cometary astropause has also been obtained in the far infrared (Ueta 2008).

The companion, Mira B, is probably a white dwarf with a temperature of ∼10^4 K (Sokoloski & Bildsten 2010) at a projected distance on the plane of the sky (measured in 2014, Ramstedt et al. 2014) of 0.487″±0.006″ from Mira A and at a position angle of 8° south of east as measured at 95 and 229 GHz on partially ionized gravitationally

* E-mail: pttnhung@vnsc.org.vn

© 2016 The Authors

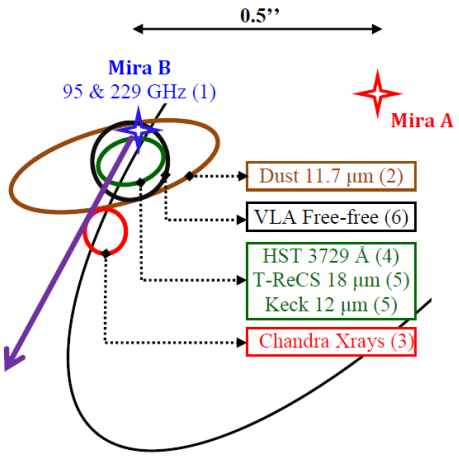

Figure 1. Schematic summary of multiwavelength emission in the Mira B environment. Data are from References 1 (Ramstedt et al. 2014; Vlemmings et al. 2015), 2 (Marengo et al. 2001), 3 and 4 (Karovska et al. 2005), 5 (Ireland et al. 2007), 6 (Matthews & Karovska 2006). The coloured ellipses are meant to give the measured position of Mira B with respect to Mira A (red star) with an estimate of the measurement uncertainties. We did not correct for the movement of Mira B with respect to Mira A during the time separating the different measurements, which were all made in the past ten years or so. The associated corrections are of the same order of magnitude as the measurement uncertainties. The magenta arrow displays the evolution of the observed CO(3-2) emission in the present analysis: for Doppler velocities between 42 and 44 km s^{-1} it stays on the nominal Mira B position and then extends south-east along the arrow for Doppler velocities between 44 and 46 km s^{-1}. The orbit, shown as a black ellipse, is that of Prieur et al. (2002).

bound gas (Ramstedt et al. 2014; Vlemmings et al. 2015; Planesas et al. 2016). The orbit is poorly constrained by observations (Prieur et al. 2002): between 1923 and today, Mira B has drifted by ∼0.6″ projected on the plane of the sky toward some 20° west of north (Fig. 1). The orbital period is estimated to be at least 500 years. The orbit is nearly circular and its projected eccentricity corresponds to an angle of ∼22° with the line of sight. Lyα fluoresced H2 emission has been observed by HST from Mira B in UV spectra (Wood et al. 2002). Mira B is known to accrete matter from Mira A, with a connection between the two stars having been observed in near UV using the HST (Karovska et al. 2005), in mid infrared using the Keck telescope (Ireland et al. 2007), in soft X rays using Chandra (Karovska et al. 2005) and in free-free emission at 8.5 GHz using the VLA (Matthews & Karovska 2006). The Chandra observation has revealed the occurrence of an X ray outburst and of intense activity in the system, also confirmed by the detection of variable OH maser emission (Etoka et al. 2010). A bipolar outflow with a wind velocity of 160±10 km s^{-1} has been revealed in the UV (Martin et al. 2007) and by the presence of knots in Hα (Meaburn et al. 2009). It makes an angle of 69°±15° with the plane of the sky, the northern jet being red-shifted and the southern jet blue-shifted (Meaburn et al. 2009).

Mira's circumstellar envelope has been observed in CO(2-1) using the Plateau de Bure interferometer (Planesas et al. 1990; Josselin et al. 2000) and in CO(1-0) using the Berkely Illinois Maryland Association interferometer (Fong et al. 2006). The former see a nearly spherical envelope disturbed north and south by the bipolar outflow while the latter suggest a kinematics combining rotation and expansion. Both quote very low expansion velocities not exceeding ±5 km s^{-1}.

Recently, the short distance environment of Mira A+B has been observed using the Atacama Large Millimetre/submillimetre Array (ALMA). Continuum emission has been observed at 1, 3 and 7 mm wavelength and its analysis (Vlemmings et al. 2015; Planesas et al. 2016), in particular in association with JVLA observations (Matthews et al. 2015), has resolved Mira A photosphere with unprecedented spatial resolution. The ^{12}CO(3-2) line emission has been mapped with an also unprecedented spatial resolution of ∼0.5″ up to a distance of ∼10″ from the central star by Ramstedt et al. (2014). The map reveals the presence of a bubble in the south-east quadrant and of a complex pattern of arcs. The authors suggest an interpretation in terms of Mira A's slow wind filling its Roche lobe and being accreted by Mira B in the orbital plane (Mohamed & Podsiadlowski 2012). In the present work we analyse other ALMA observations that have recently been open to public access and offer a slightly better resolution at short distance from the pair of stars. While not repeating in any way the analysis of Ramstedt et al. (2014) our analysis provides a useful complement to their work by using different approaches and concentrating on different issues. In particular the better spatial resolution of the present data makes it possible for us to study the short distance environment of the binary in considerably more detail than available in Ramstedt et al. (2014).

2 OBSERVATIONS AND DATA REDUCTION

We consider here a set of observations (ADS/JAO.ALMA/2013.1.00047.S), made on the CO(3-2) line between 12 and 15 June 2014 with configurations including between 34 and 36 antennas and having a maximal baseline of 650.5 km. The data have been reduced, merged and corrected for the primary beam by the ALMA staff to clean maps using pixel sizes of 0.06″×0.06″ and having a beam of angular dimensions of 0.325″×0.309″ FWHM at position angle of 83.2°. The total time on source was ∼10.6 minutes. The line Doppler velocity spectrum evaluated from 25 km s^{-1} to 65 km s^{-1} is available in channels of 0.4 km s^{-1}.

We define y and z as coordinates in the plane of the sky, y pointing east and z pointing north. The projected angular distance of pixel (y, z) from the origin is $R = \sqrt{y^2 + z^2}$ and its position angle, measured clockwise from west, is $\varphi = \arctan(z/y) + \pi$. The x axis is parallel to the line of sight with positive x values being red-shifted. The measured flux density is $f(y, z, V_x)$ and its integral over the measured Doppler velocity V_x, normally between 34 km s^{-1} and 56 km s^{-1}, is $F(y, z) = \int f(y, z, V_x) dV_x$. We define an effective emissivity $\rho = f(y, z, V_x) dV_x/dx$, that mixes information concerning both gas density and temperature.

A study of the evolution of the distribution of the measured flux density when moving away from the star reveals a strong dependence on the velocity channel of the effective

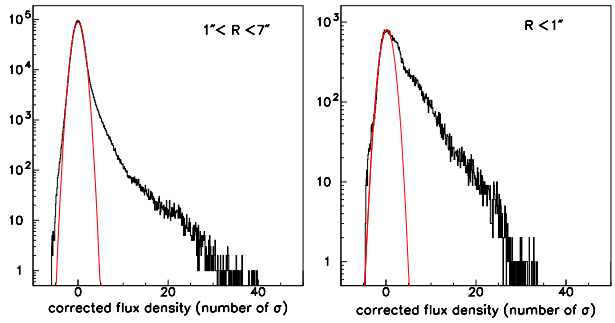

Figure 2. Distributions of $[f(y,z,V_x) + \Delta f(V_x)]/\sigma_f(V_x)$ for $1''<R<7''$ (left) and, after having increased $\Delta f(V_x)$ by 0.04 Jy arcsec^{-2} and $\sigma_f(V_x)$ by 30%, for $R<1''$ (right). The Gaussians have unit variance and are centred at the origin.

noise (meaning the peak observed at the lower flux densities). Indeed, as noted and explained by Ramstedt et al. (2014) using a similar set of observations, the effective noise peaks at different values and displays different widths in different velocity channels, the channels with strong emission having a limited dynamic range due to the lack of large distance coverage. We therefore evaluate, for pixels distant from the star by a projected angular distance $1''<R<7''$ and for each velocity channel separately a shift $-\Delta f(V_x)$ and a width $\sigma_f(V_x)$ from a Gaussian fit to the effective noise peak. The resulting distribution of $[f(y,z,V_x) + \Delta f(V_x)]/\sigma_f(V_x)$ is shown in Fig. 2 (left). However, when looking at the same quantity in the star region ($R<1''$), we find that we need to increase $\sigma_f(V_x)$ by ∼30% and $\Delta f(V_x)$ by ∼0.04 Jy arcsec^{-2} in order to obtain a good description of the effective noise (Fig. 2 right). Typically, going from low to high emission, $\sigma_f(V_x)$ increases from less than 0.1 to ∼0.6 Jy arcsec^{-2} and $\Delta f(V_x)$ from zero to ∼0.15 Jy arcsec^{-2}. We estimate that both quantities are obtained with an uncertainty of the order of 30% of their value. In what follows, flux densities are corrected accordingly and are retained only if they exceed a specified number of $\sigma_f(V_x)$, usually 2 (we speak of a cut at 2σ's). We have checked systematically that all results presented here are not significantly affected by a change in the cut level, or even by the absence of cut.

The distribution of F as a function of R, averaged over position angles and integrated between 34 km s^{-1} and 56 km s^{-1} is displayed in Fig. 3 (left) for cuts at 1, 2 and 3 σ's. In what follows, we restrict accordingly the analysis to pixels having $R<7''$ in order to be free of problems related with the lack of large distance coverage. In practice, most of the results presented here are confined to the interior of a circle of radius $R=3''$. Distributions of F as a function of y and z are then shown in Fig. 3 (middle and right) for cuts at 1, 2 and 3σ's. They have been centred to have the peak of maximum emission at the origin of coordinates.

Channel maps covering $8.2'' \times 8.2''$ are shown in Appendix A.

3 MORPHOLOGY AND KINEMATICS OF THE CIRCUMBINARY ENVELOPE: AN OVERVIEW

Maps of the integrated flux, F, and of the mean Doppler velocity, $<V_x>$, are displayed in Fig. 4 for a cut at 2σ's. It is tempting to associate regions having similar Doppler velocities and to group them to form simple patterns. An example is a large south-eastern arc, labelled B in Fig. 4, corresponding to what Ramstedt et al. (2014) call a bubble. While the reality of such associations needs to be critically assessed, one can state that a distinctive feature of the data is the existence of regions separated by several arcseconds but sharing very similar Doppler velocities. Fig. 5 displays the Doppler velocity distribution in a circle of radius $7''$ centred on Mira A. It shows the contribution of several peaks giving evidence for distinct families of sources, making it easier to cope with the complexity of the observed patterns, which Ramstedt et al. (2014) have rightly mentioned as being an essential feature of the Mira environment.

Channel maps in velocity intervals representative of the structure observed in Fig. 5 are shown in Fig. 6. The blue shifted region, 34 to 44 km s^{-1}, and the red-shifted region, 50 to 56 km s^{-1}, respectively identified by Ramstedt et al. (2014) as dominated by a bubble and by spiral arcs, will be treated separately from the central velocities, 44 to 50 km s^{-1}, that correspond to sources confined inside a circle of ∼2.5″ radius around Mira A. The three velocity intervals just mentioned are not perfectly separated, which complicates the analysis in the overlap regions. We shall aim at giving as objective as possible a description of what has been observed, without relying on a priori preconceptions, such as the existence of spiral wakes or of an accretion disk around Mira B. The complexity of the observed patterns is such that one can easily be induced into grouping different features in associations that may have no real identity. Moreover, the emission of the CO(3-2) line traces the presence of gas in only well-defined conditions of temperature, is strongly influenced by the presence of turbulences or of short wavelength radiations and is sensitive to optical thickness. In the very variable and inhomogeneous environment of Mira, such factors may well play an important role.

4 THE BLUE-SHIFTED SOUTH-EASTERN BUBBLE

Figure 7 (left) displays the sky map of F integrated between Doppler velocities of 34 and 44 km s^{-1}. Two ellipses have been drawn by eye to roughly delineate the pattern identified by Ramstedt et al. (2014) as a bubble. The position angle of the major axis is 17° north of west, the aspect ratio (ratio of major to minor axes) is 1.5, the half minor and major axes measure 4.1″ and 5.5″ respectively and the coordinates of the centre are $y = 4.8''$ and $z = -3.3''$. We define for each point (y,z) in the plane of the sky an elliptic radial coordinate η cancelling at the centre of the ellipse and taking respective values of 0.85 and 1.15 on the two ellipses of Fig. 7:

$$\begin{aligned} \xi &= (y-4.8'')\cos(17^\circ) - (z+3.3'')\sin(17^\circ) \\ \zeta &= (y-4.8'')\sin(17^\circ) + (z+3.3'')\cos(17^\circ) \\ \eta^2 &= (\tfrac{\xi}{7.2''})^2 + (\tfrac{\zeta}{4.8''})^2 \end{aligned} \quad (1)$$

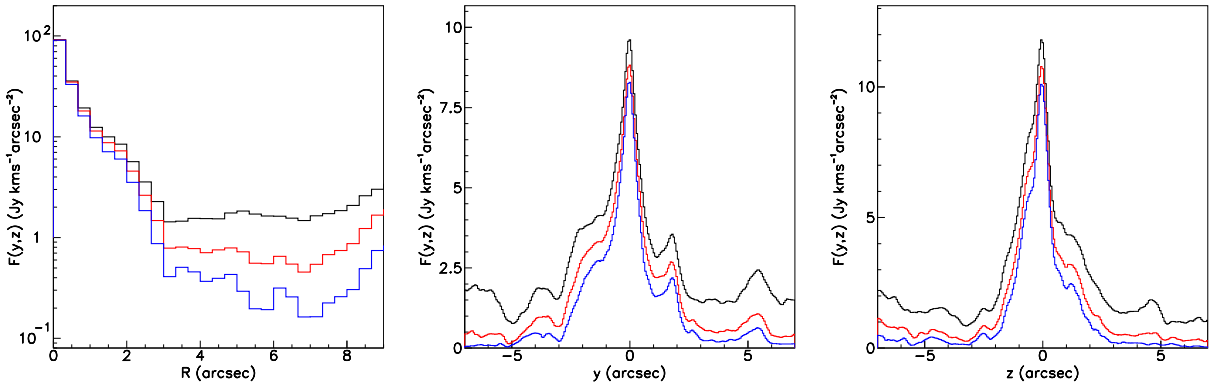

Figure 3. Left: distributions of $F(y, z)$ as a function of R. Middle and right: distributions of $F(y, z)$ as a function of respectively y and z for $|y|<7''$ and $|z|<7''$. Colours indicate cuts at 1 (black), 2 (red) and 3 (blue) σ's.

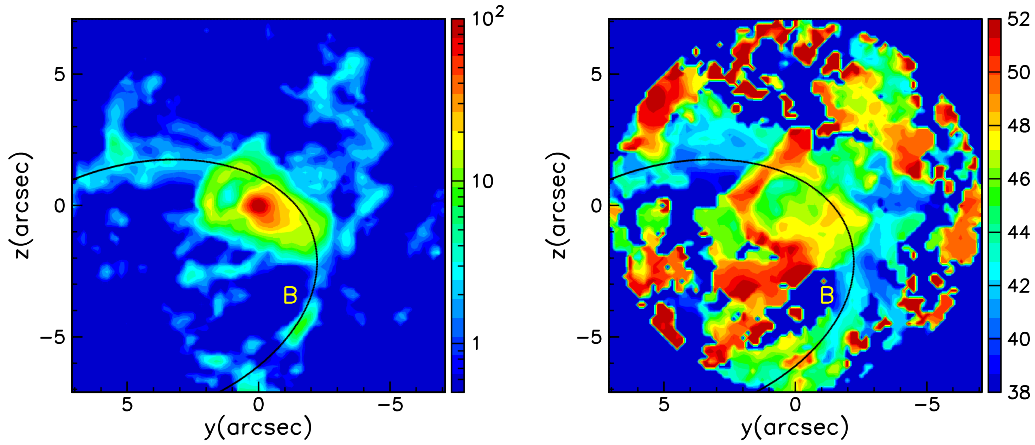

Figure 4. Maps of F (left, Jy km s^{-1}arcsec^{-2}) and $<V_x>$ (right, km s^{-1}) for a cut at 2σ's. The curve labelled B corresponds to the bubble (see text).

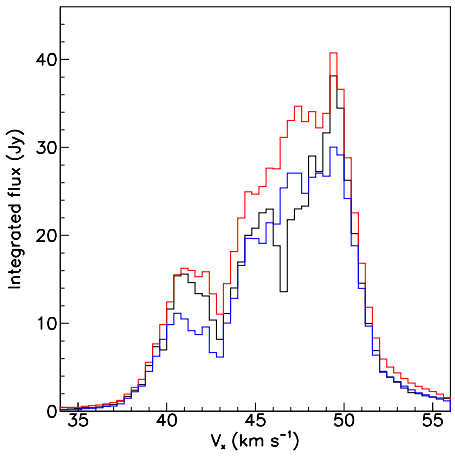

Figure 5. Doppler velocity distributions in a circle of radius $7''$ centred on Mira A for cuts at 2σ's (red) and 3σ's (blue) or without any cut (black).

We also define an elliptical position angle φ_{bubble}, measured clockwise from east (rather than from west) such that $\tan(\varphi_{bubble}+17^\circ) = (\zeta/4.8'')/(\xi/7.2'')$. In order to keep away from contributions from the Mira A+B neighbourhood we require φ_{bubble} not to be in the interval [120°,155°].

Figure 7 (middle) displays the flux per pixel and velocity bin averaged over φ_{bubble} as a function of η. The bubble region sticks out very clearly. The FWHM is 0.17, meaning $\sim$1.0$''$ on average. The inner edge is sharper than the outer edge, while the opposite is expected from a bubble (understood as an ellipsoid shell of constant thickness). The inner region is strongly depleted, at the limit of sensitivity when using a cut at 2σ's (as done here). The ratio of the flux integrated over the inner part of the bubble (η <0.8) to the flux integrated over the periphery of the bubble (0.8< η <1.4) is 2.8% with a 2σ cut and 7.4% without cut. Figure 7 (right) displays the Doppler velocity distribution for pixels having η <0.8$''$ and pixels having 0.8$'' < \eta <$1.4$''$ separately.

The dependence of the mean Doppler velocity $<V_x>$ on η and φ_{bubble} is illustrated in Fig. 8 and shows small, but significant variations. The mean Doppler velocity increases

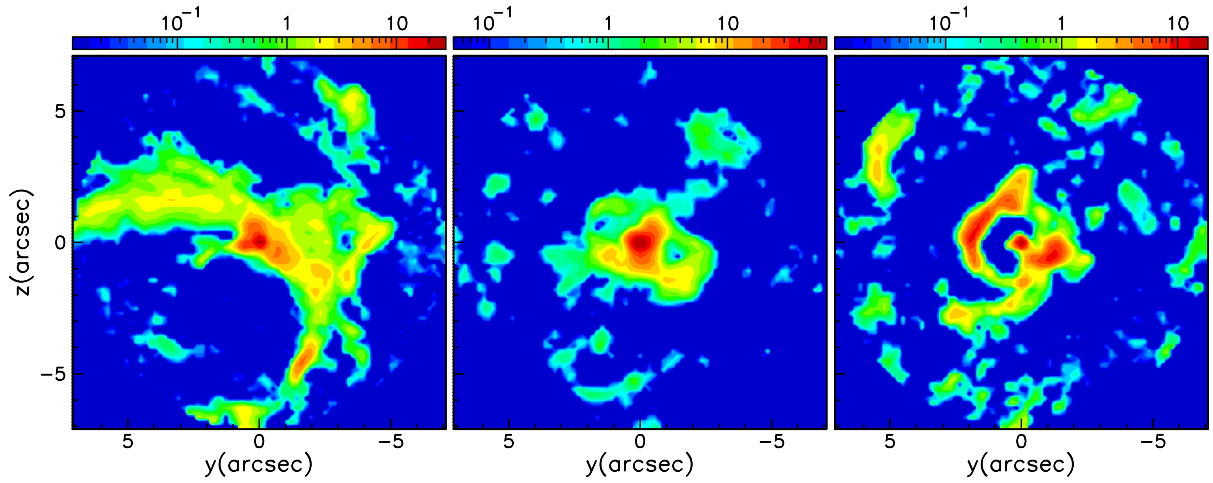

Figure 6. Channel maps drawn inside a 7″ radius circle centred on Mira A for a 2σ cut, with velocity intervals of 34-44, 45-49 and 50-56 km s^{-1} from left to right. The colour scale is in the unit of Jy km s^{-1} arcsec^{-2}

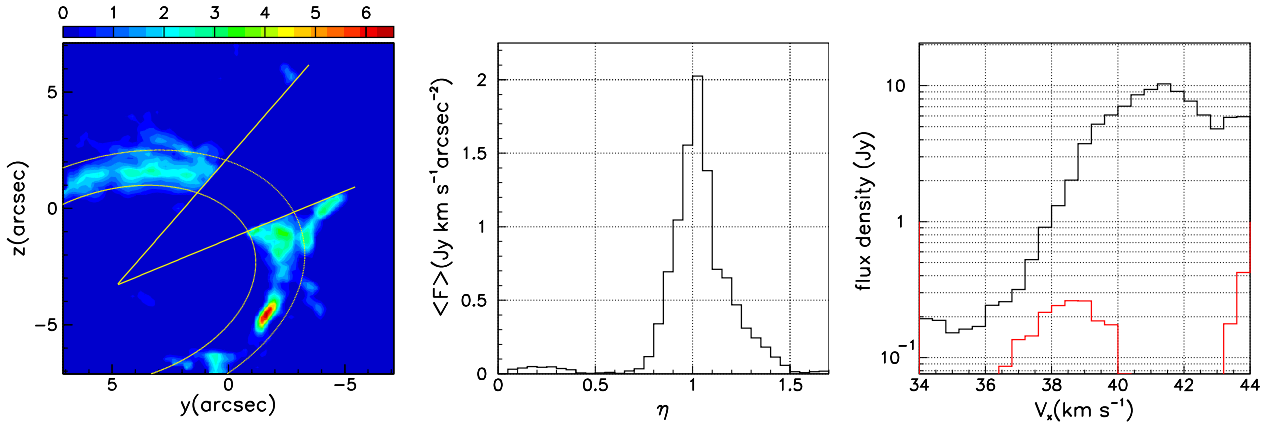

Figure 7. Left: Sky map of F (Jy km s^{-1} arcsec^{-2}) integrated between Doppler velocities of 34 and 44 km s^{-1}. The ellipses correspond to η=0.85 and 1.15, the lines to φ_{bubble}=120° and 155°. Middle: Flux density averaged over φ_{bubble} as a function of η. Right: Doppler velocity distribution for pixels having η<0.8 (red) and pixels having 0.8<η<1.4 (black) separately.

from ∼39 km s^{-1} inside the arc to between 41 and 42 km s^{-1} on the arc and beyond. In the arc region, it increases from ∼40 km s^{-1} at the north-eastern extremity to between 42 and 43 km s^{-1} at the south-western extremity. If the ellipse is interpreted as the projection of a circular ring in space, its angle with the plane of the sky is ∼50°. Moreover, if the ring is expanding radially at constant velocity, as suggested by Fig. 8 (right), this constant velocity would project as (42.5−40.0)/2∼1.3 km s^{-1} on the line of sight, namely would be of the order of 1.7 km s^{-1} in space. To span 7.2″, meaning ∼720 AU, at such velocity takes ∼2000 yr.

In summary, the blue-shifted part of the Doppler velocity distribution is dominated by a narrow arc (∼1″ FWHM), referred to as "the bubble", that can be interpreted as the projection of a circular ring expanding at a velocity of less than 2 km s^{-1}, born some 2000 years ago and making an angle of ∼50° with the plane of the sky.

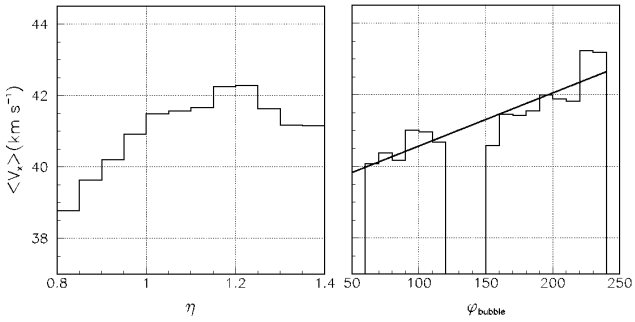

Figure 8. Dependence of the mean Doppler velocity <V_x> on η (left) and, for the bubble region defined as 0.8<η<1.4, on φ_{bubble} (right, measured clockwise from east).

5 RED-SHIFTED ARCS

Figure 9 (left) displays the sky map of F integrated over Doppler velocities larger than 48 km s^{-1}. It shows several zones of emission, the main ones being labelled A1, A2, A3 and A4 for further reference. The region surrounding Mira A+B at distances not exceeding 2.3″ is treated in the next section.

The right panel displays the Doppler velocity distribution in the region 2.3″<R<7″, the red histogram showing the contribution of what is described as the south-western outflow in the next section. Two peaks, at ∼41.5 and ∼49.5 km s^{-1}, stand out, suggesting a global expansion about a mean velocity of ∼45.5 km s^{-1}. The blue peak is easily identified as the contribution of the bubble, the red peak being associated with the arcs displayed in the left panel. We have considered various possible associations of these sources, either on spiral arms or on large circles or ellipses. We do not feel confident enough to give sufficiently convincing arguments about their physical reality and we prefer to refrain from doing so. This should not be understood as a statement against the existence of such associations, but we are simply unable to unravel them with sufficient confidence from the present data. The data used by Ramstedt et al. (2014), having a better coverage at large distances are more suitable for this purpose than those used here.

6 THE CLOSE ENVIRONMENT OF THE MIRA A+B PAIR

6.1 Immediate environment

From the parameters of the Mira B orbit derived by Prieur et al. (2002) we evaluate the space velocity of Mira B in the Mira A rest frame to be ∼5.0 km s^{-1} and the Doppler shift between the two stars to be ∼1.0 km s^{-1}. Fig. 10 shows Doppler velocity distributions in the immediate environments of Mira A and B respectively.

Near Mira A, the spectrum is asymmetric, with the blue tail larger than the red tail. This cannot be due to the contribution of the bubble, which is quite small and indeed clearly identified at ∼42 km s^{-1}. The spectrum can be described in terms of two Gaussian components: one, narrow (FWHM=3.9 km s^{-1}) centred at 47.2 km s^{-1} and a wider one (FWHM=10.5 km s^{-1}) centred at 45.7 km s^{-1}. Integrating over velocity, the former is 40% larger than the latter. If the broader component were caused by radial expansion, it would mean an expansion velocity of ∼5 to 10 km s^{-1}, at the scale of the space velocity of Mira B in the Mira A rest frame. The 1.5 km s^{-1} difference between Mira A and the centre of expansion could then be interpreted as the result of the centre of mass of the circumbinary envelope being blue-shifted by such an amount with respect to the current velocity of Mira A. If such were the case, Mira B would therefore be blue-shifted with respect to Mira A and closer to the Earth than Mira A.

Near Mira B (Fig. 10 middle) the spectrum displays two peaks, one peaking at 47.9 km s^{-1} and the other at 44.6 km s^{-1}. The relative amplitude of the two peaks is not strongly dependent on the size of the circle over which the flux density is integrated around Mira B. This is also illustrated in Fig. 11, which displays position-velocity diagrams confined to the immediate environment of Mira A and B respectively. In the present work, we call position-velocity (P-V) diagram a distribution in a plane spanned by the Doppler velocity and one of the sky coordinates, Cartesian or polar or else, of the flux density averaged over the other sky coordinate. The emission centred on Mira B covers Doppler velocities from ∼41 to ∼46 km s^{-1} (here, again, the contribution from the bubble is small, even if relatively larger than in the preceding Mira A case). Moreover, it is spatially resolved and extends over several tenths of an arcsecond (the beam has a σ of ∼0.13″).

The extension found by Vlemmings et al. (2015) in the continuum is only 0.026″ FWHM, significantly smaller than what is seen here. It is worth recalling on this occasion that such dimensions are much larger than what is expected from the accretion disk, which is far from being detectable. The emission detected in the present study, is from molecular carbon monoxide, implying temperatures at the 100 K scale, and a low density of short wavelength radiations that dissociate molecules. The emission detected in the continuum by Vlemmings et al. (2015) at ∼95 and ∼229 GHz is from partially ionized, gravitationally bound gas, namely much closer to Mira B than in the present case (and still farther away than the accretion disk).

The difference between the fluxes integrated in circles of 0.3″ radius around Mira B and its symmetric with respect to Mira A (y=−0.5″, z=0.07″) is displayed in the right panel of Fig. 10. If the peak at 44.5 km s^{-1} seen in the middle panel were due exclusively to gas gravitationally bound to Mira B, the difference spectrum would also peak at 44.5 km s^{-1} above a zero baseline and reveal the emission associated with the bound gas. Instead, it peaks at 43.6 km s^{-1}, 1 km s^{-1} lower, and becomes negative between ∼45.5 and 50 km s^{-1}. This implies that rather than seeing gas gravitationally bound to Mira B, we rather see an asymmetry of the gas flowing from Mira A, with an enhancement in the direction of Mira B, namely eastward and toward the Earth.

A close look at the immediate environment of Mira A+B between 41 and 46 km s^{-1} is given by the channel maps displayed in Fig. 12. Up to 44 km s^{-1}, the emission is approximately centred on Mira B but for higher Doppler velocities it evolves into a south-eastern arm that may be interpreted as an outflow having its source at Mira A and flowing toward negative x values, being eventually focused by Mira B. At the same time, two other outflows seem to originate from Mira A, one aiming south-west and the other aiming some 20° east of north. They will be discussed in the following sections.

Another illustration is given in Fig. 13, which displays P-V diagrams over adjacent y strips, each two pixels wide (0.12″), z being used as space coordinate. In addition to easily identifiable contributions from the bubble and from red-shifted arcs, they show the south-eastern arm and the north-eastern arm just mentioned. The north-eastern arm covers Doppler velocities between ∼42.5 and ∼45.5 km s^{-1} in the north-eastern quadrant of the sky map, with both y and z reaching to ∼1″ from Mira A. On average, it is blue-shifted by 3.5 km s^{-1} with respect to Mira A; if assigned to a wind having an expansion velocity of ∼7 km s^{-1}, this would imply an angle of ∼60° with the line of sight.

In the southern hemisphere, the P-V diagrams having y<0.5″ are dominated by the south-western outflow;

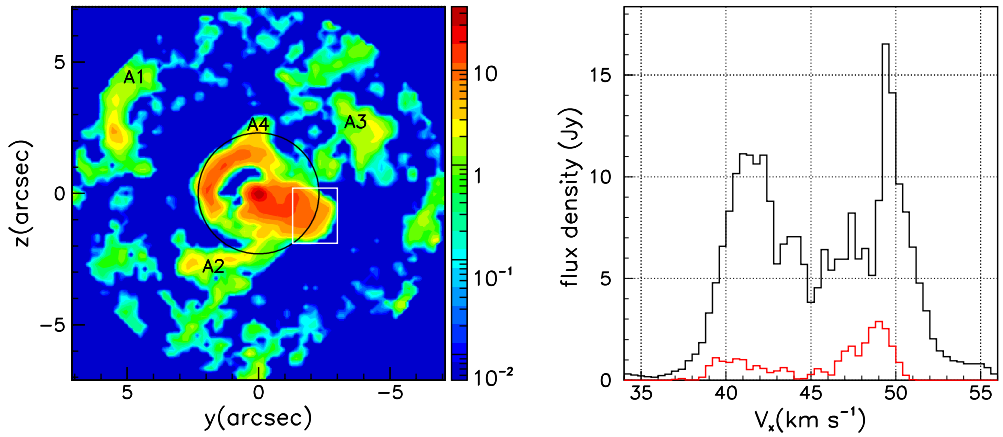

Figure 9. Left: Sky map of F (Jy km s^{-1} arcsec^{-2}) for Doppler velocities V_x>48 km s^{-1}. Right: Doppler velocity distributions for pixels located outside a circle centred on Mira A and having a radius of 2.3″, as shown on the left panel. The red histogram displays the contribution of the flux contained in the part of the rectangle exterior to the circle (on the left panel).

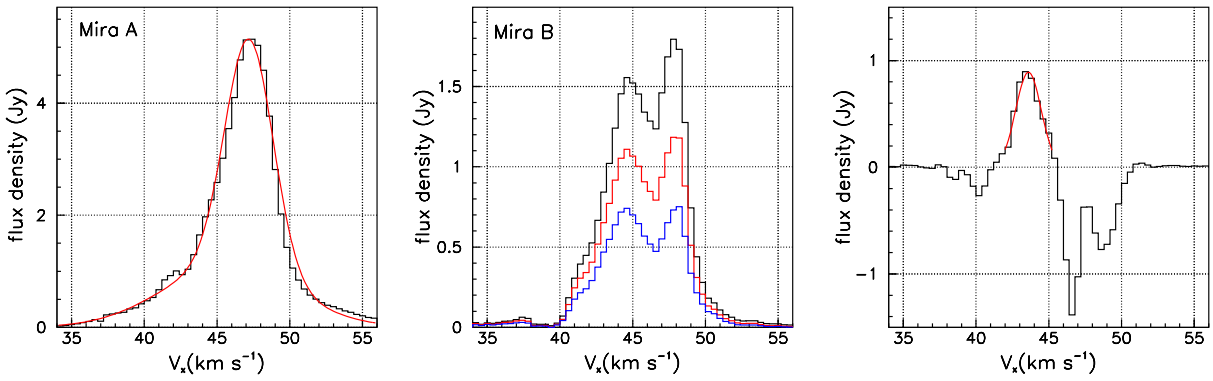

Figure 10. Left: Doppler velocity distribution integrated in a circle of radius 0.3″ centred on Mira A. The fit is the sum of two Gaussians (see text). Middle: Doppler velocity distributions integrated in circles of radius 0.20″ (blue), 0.25″ (red) and 0.3″ (black) centred on Mira B. Gaussian fits to the peaks for the 0.20″ radius give mean velocities of 44.6 and 47.9 km s^{-1}, amplitudes of 0.73 and 0.74 Jy arcsec^{-2} and σ's of 1.6 and 1.1 km s^{-1}. Right: difference between the Doppler velocity distributions integrated in circles of radius 0.3″ and centred on Mira B and on the symmetric of Mira B with respect to Mira A. The curve is a Gaussian fit to the peak with mean value of 43.6 km s^{-1}, FWHM of 2.0 km s^{-1} and amplitude 0.89 Jy arcsec^{-2}.

however, from Mira B onward, one sees the south-eastern arm starting to develop, covering Doppler velocities between ∼43.5 and ∼46.5 km s^{-1}. At the same time, as y increases, the contribution of the south-western outflow fades away. The projected velocity on the plane of the sky of Mira B with respect to Mira A is ∼3 km s^{-1}. The mean Doppler velocity of the south-eastern arm is ∼45 km s^{-1}, blue-shifted by 2.5 km s^{-1} with respect to Mira A; again, if assigned to a wind having an expansion velocity of ∼7 km s^{-1}, this would imply an angle of ∼70° with the line of sight and a velocity of ∼6 km s^{-1} in the plane of the sky. If the interpretation of the south-eastern arm as an outflow having its source at Mira A and being focused by Mira B is correct, the combined movements of the expanding gas and of the orbiting Mira B would generate a small southward curvature of the south-eastern arm compatible with what is observed.

In summary, the observation between Doppler velocities of 42 and 44 km s^{-1} of an enhanced emission at the precise location of Mira B (Fig. 12) gives evidence for the white dwarf to play an important role in shaping the morphology and kinematics of the gas flow in its environment. The evolution of the P-V diagrams displayed in Fig. 13 east of Mira B provides another illustration adding to this evidence. At first sight, one might think that we are observing a mass of gas surrounding Mira B, with a size of a few tens of AU, and having Doppler velocities with respect to Mira B reaching 1.5 km s^{-1} in each of the red and blue directions. In this case, the velocity dispersion would be the result of rotation or/and accretion or/and thermal agitation. The P-V

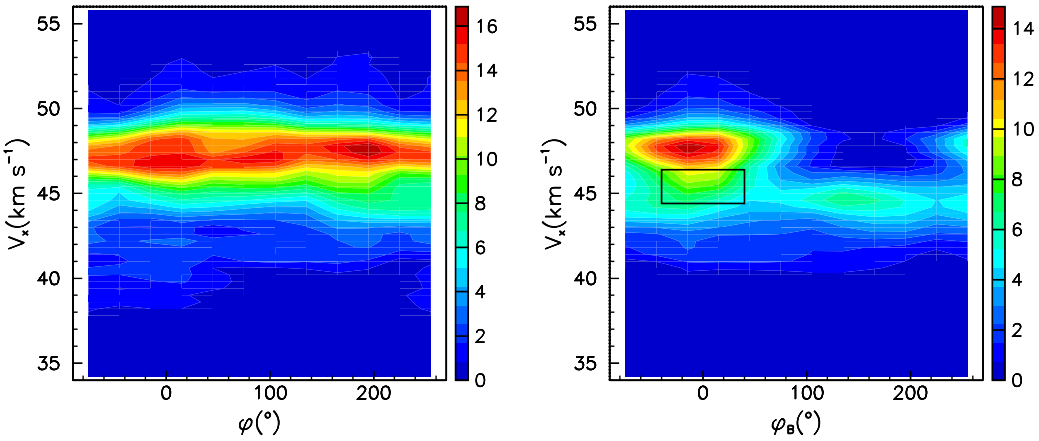

Figure 11. Position-velocity diagrams centred on Mira A (left) and on Mira B (right). The abscissas are the position angles φ and φ_B measured clockwise from west around Mira A and B respectively. The Mira A diagram is for radii contained in the interval [0.1″,0.4″] and the Mira B diagram for radii contained in the interval [0.05″,0.30″]. The colour scale is in the unit of Jy arcsec^{-2}. The rectangle in the right panel ($44.4<V_x<46.4$ km s^{-1} and $-40°<\varphi_B<40°$) corresponds to flux densities mapped in the left panel of Fig. 14.

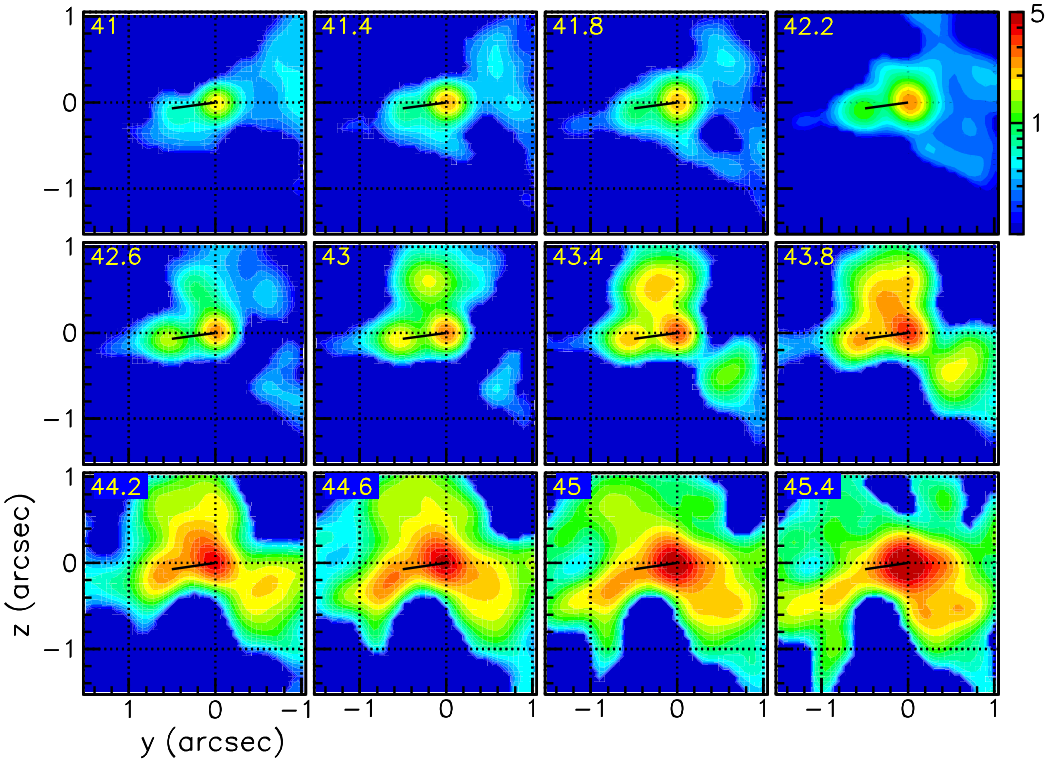

Figure 12. Channel maps starting at 40.8 km s^{-1} and ending at 45.6 km s^{-1} in successive 0.4 km s^{-1} wide channels. Each panel is labelled with the central velocity (km s^{-1}). The colour scale is in the unit of Jy km s^{-1} arcsec^{-2}. Black lines show the relative positions of Mira A and Mira B.

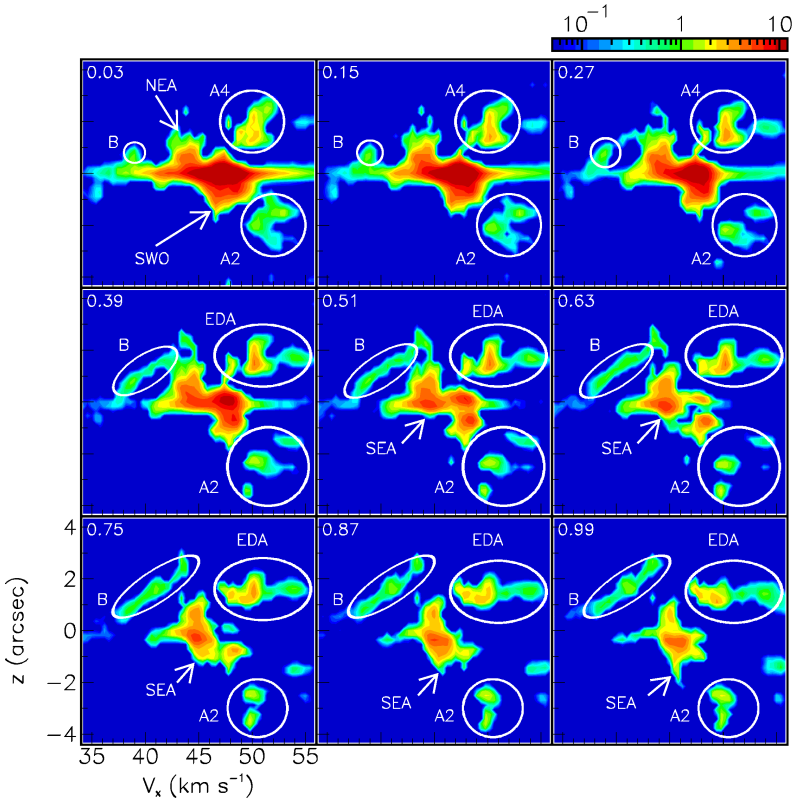

Figure 13. P-V diagrams over adjacent y strips, each two pixels wide (0.12″), z being used as space coordinate. Each panel is labelled with the central value of y. The contributions of the bubble (B) and of red-shifted arcs (A2, A4, see Fig. 9, and Eastern Detached Arm, see section 6.2 and Fig. 20) are indicated. Also shown, on the first panel, are the contributions of the north-eastern arm (NEA) and of the south-western outflow (SWO). Starting from panel 5, yellow arrows point to the developing south-eastern arm (SEA).

diagram of Fig. 11 (right) could reveal a rotation only if its axis were significantly inclined with respect to the line of sight and a bipolar flow only if its axis were significantly inclined with respect to the plane of the sky. It does not show any clear sign of such effects but better spatial and spectral resolutions would be necessary to place sensible limits on the corresponding velocities. Moreover, if we were observing gas gravitationally bound to Mira B, one would need to assume that the orbit of Prieur et al. (2002) predicts a Doppler shift between Mira A and B three times smaller than what it really is.

It seems therefore more plausible to assume that we are seeing gas flowing from Mira A toward Mira B, being eventually focused or even partly trapped by Mira B. More precisely, the gas flow emitted by Mira A in a solid angle facing Mira B, therefore blue-shifted, concentrates toward Mira B very much as predicted by Model 1 of Mohamed & Podsiadlowski (2012) in the framework of their Wind Roche Lobe Overflow (WRLOF) picture. The velocity distribution displayed in the right panel of Fig. 10 gives strong support to this interpretation. While it is sensible to assume that the gas ejected from Mira A, and attracted and eventually trapped by Mira B, will ultimately be accreted, none of this can be seen from the present data (and is not expected to). The evidence for the gas flow to be enhanced in the neighbourhood of Mira B does not exclude a possible small contribution of gravitationally bound gas, but the present observations prevent to quantify it reliably. A hydrodynamic model of the gravitational attraction and focalization produced by Mira B would help a better understanding of the dynamics at play.

Finally, Fig. 14 provides additional information related to the P-V diagrams of Fig. 11. The left panel maps the flux in the rectangle displayed in the right panel of Fig. 11, at Doppler velocities intermediate between the Mira A and Mira B maxima, showing that emission is dominated by Mira A but slightly shifted toward Mira B. The middle panel displays the dependence on position angle measured with respect to Mira A of the Doppler velocity averaged in a circle centred on Mira A for distances between 0.1″ and 0.6″ and $45<V_x<50$ km s^{-1}. The sine wave fit corresponds to a bipolar outflow of ±0.15 km s^{-1} amplitude pointing north and south, with a mean value of 47.4 km s^{-1}. When retaining only pixels closer to the star, the amplitude of the oscillation decreases but the mean velocity and the phase shift are unaffected. The right panel displays the dependence on R of the mean Doppler velocity $<V_x>$ averaged over position angle in the eastern hemisphere (toward Mira B) and the western hemisphere separately. While starting together at $\sim$47 km s^{-1} they quickly depart from each other: the eastern part is first blue-shifted with respect to the western part but, beyond $\sim$1.5″, the reverse applies.

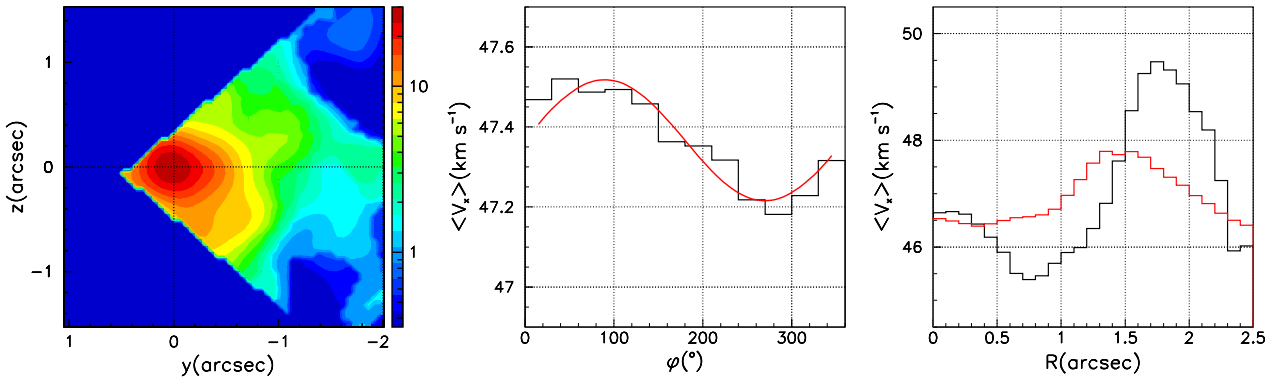

Figure 14. Left: Sky map of the flux densities contained inside the rectangle drawn in the right panel of Fig. 11. Middle: Dependence on position angle measured with respect to Mira A of the Doppler velocity averaged in a circle centred on Mira A for distances between 0.1″ and 0.6″ and 45<V_x<50 km s^{-1}. The sine wave fit corresponds to a bipolar outflow of ±0.15 km s^{-1} amplitude pointing south, with a mean value of 47.4 km s^{-1}. Right: Distribution of <V_x> on R, averaged over east (black) and west (red) position angles separately.

6.2 An overview at larger distances

When looking on a larger scale (Fig. 15 left), in a radius of 3″ around Mira A and excluding the blue-shifted and red-shifted ends of the Doppler velocity spectrum, emission is enhanced along a direction pointing some 30° south of west over a broad range of position angles. We refer to this enhancement as the south-western outflow. Facing it, pointing to some 30° north of east (defined as z' axis), another enhancement displays a strong central depression, reaching up to ∼1.5″ projected distance from Mira A. We refer to it as the north-eastern outflow. When averaging over position angles, the integrated flux decreases smoothly with radius in the south-western outflow but is steeper at short distances and strongly enhanced between 1.5″ and 2″ in the north-eastern outflow (Fig. 15 middle). Similarly, the mean Doppler velocity remains confined between 47 and 48 km s^{-1} in the south-western outflow but is strongly blue-shifted at short distances, around 1″, and strongly red-shifted at large distances, around 2″ in the north-eastern outflow (Fig. 15 right). When averaging instead over R the position angle distribution displays a south-west to north-east ratio in excess of 2 for 0.5″<R<1.5″, but is better equilibrated between south-west and north-east for 1.5″<R<2.5″ (Fig. 16 left). Similarly, the mean Doppler velocity displays a strong north-east to south-west asymmetry for 0.5″<R<1.5″, decreasing abruptly from ∼48 km s^{-1} west to ∼46 km s^{-1} east, but is better equilibrated between south-west and north-east for 1.5″<R<2.5″ (Fig. 16 middle).

In order to reveal a possible rotation about the approximate axis of symmetry z', we display in Fig. 16 (right) the distribution on the perpendicular axis, y', of the mean Doppler velocity averaged over −2″<z'<2″ or −1″<z'<1″ and 42<V_x<53.2 km s^{-1}. In both z' intervals we find no clear evidence for rotation. However, in the central region (|y'|<1″,|z'|<1″) the data can accommodate a rotation of ∼ ±0.5 km s^{-1} arcsec^{-1}.

Figure 17 displays a P-V diagram averaged over 0.5″<R<2.5″ using the position angle φ as space coordinate. The western outflow covers from ∼60° north of west to ∼30° east of south, where its limbs are seen to share similar Doppler velocities around 47 km s^{-1}, and has an axis close to the plane of the sky, pointing ∼30° south of west, where Doppler velocities span from ∼43 to ∼52 km s^{-1}, meaning a radial expansion velocity of at least 5 km s^{-1}. The eastern outflow, displays an atypical pattern with two nearly separated arms, one blue-shifted and pointing between east and south-east, the other red-shifted covering the north-eastern quadrant.

Sky maps associated with distinct regions of emission identified in the P-V diagram of Fig. 17 are displayed in Fig. 18. Regions 1 and 2 cover the south-western outflow but region 2 extends about twice as far from Mira A than region 1 does, emission being enhanced at larger distances from the star. While region 4 faces region 1 and displays a similar morphology, regions 5 and 7 face region 2 but populate only large distances from the star, in excess of ∼1.5″, at variance with region 2. The Doppler velocity distribution in the part of region 2 having R>1.3″ is precisely the same as in the part having R<1.3″. Region 4 corresponds to the south-eastern arm and region 6 to the north-eastern arm that were identified in Fig. 12, the former flowing across Mira B and the latter connecting to Mira A at Doppler velocities of the order of 44 km s^{-1}.

It is not clear whether region 3 has an identity of its own or is simply the southern limb of the south-western outflow. To answer this question we show in Fig. 19 maps of the relevant region for blue-shifted and red-shifted Doppler velocities separately. The southern limb is seen to point south and to significantly overflow in the eastern hemisphere, making the case for treating region 3 separately from region 2 very weak.

P-V diagrams have the advantage of offering a visual representation of the information contained in the Doppler velocity and therefore helping with the conception of a 3-D representation of the morphology. Another approach in the same spirit is illustrated in Fig. 20, displaying a 3-D representation of the detected emission assuming radial expansion of the circumbinary envelope at constant velocity V_{rad}. In such a case, at any point (x, y, z) the relation V_x/V_{rad} =

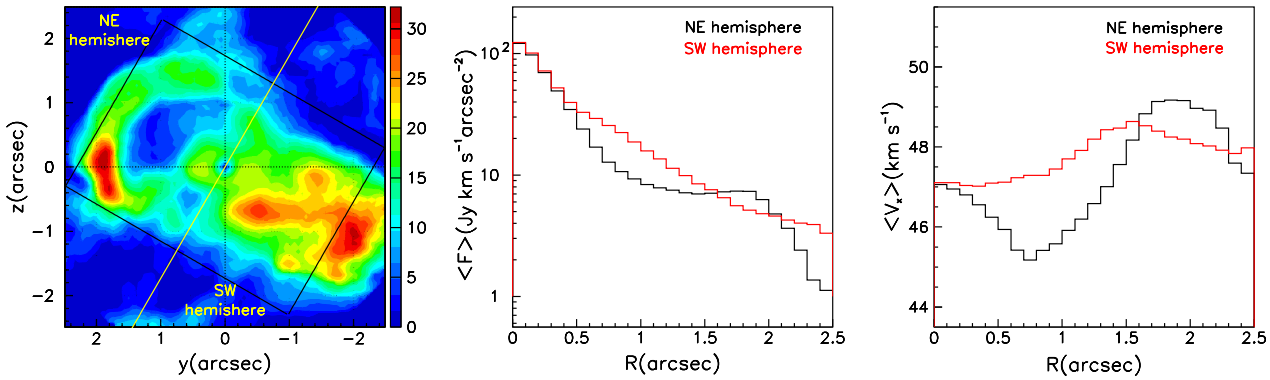

Figure 15. Left: sky map of the product $F \times R$ integrated over Doppler velocities in the range $R<3''$ and $42<V_x<53.2$ km s^{-1}. The rectangle is the region within which rotation is being looked for in the right panel of Fig. 16. Middle: radial distribution of F averaged over position angle in the same range, separately in the north-eastern (black) and south-western (red) hemispheres (defined with respect to an axis y' pointing 30° east of south, see left panel). Right: radial distribution of $<V_x>$ averaged over position angle in the same range and with the same convention.

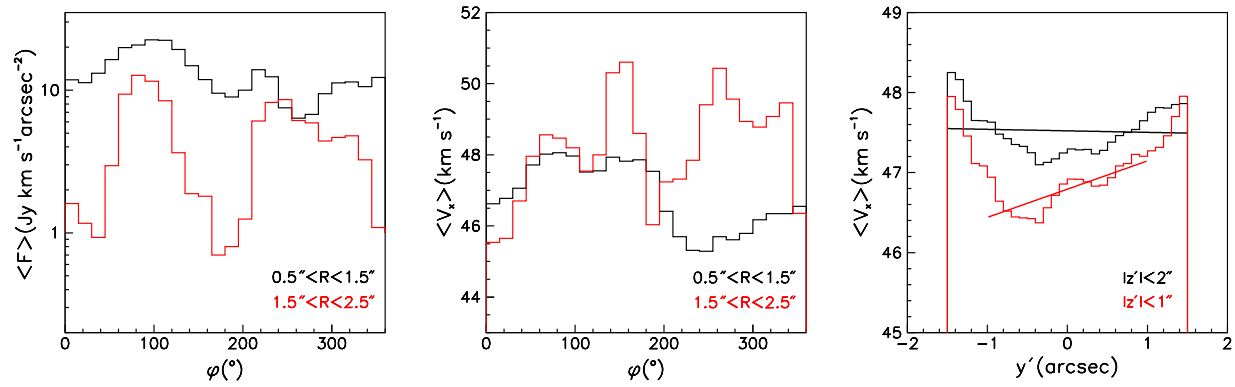

Figure 16. Left: distribution on position angle (measured clockwise from west) of the flux integrated over $42<V_x<53.2$ km s^{-1} and averaged over $0.5''<R<1.5''$ (black) or $1.5''<R<2.5''$ (red); Middle: distribution of $<V_x>$ averaged over R in the same ranges and with the same convention. The position angle is measured clockwise from 60° north of west. Right: distribution of the mean Doppler velocity as a function of $y' = -z\cos(30°) + y\sin(30°)$ averaged over $|z'|<2''$ (black, rectangle shown in the left panel of Fig. 15) or $|z'|<1''$ (red) with $z' = y\cos(30°) + z\sin(30°)$. The lines are linear fits to y' intervals $|y'|<1.5''$ (black) or $|y'|<1''$ (red) respectively.

$x/\sqrt{x^2+R^2}$ applies, meaning $x = R\,V_x/\sqrt{V_{rad}^2 - V_x^2}$. Writing $\xi = \sqrt{x^2+y^2}$ one can then image the effective emissivity in any (z,ξ) plane making an angle ω with the y axis by multiplying the measured flux density by $dV_x/dx = V_{rad}R^2(x^2+R^2)^{-3/2}$ and $dx\,dy/(d\xi\,d\omega) = \xi$. In Fig. 20, V_{rad}=7 km s^{-1}, all Doppler velocities being measured with respect to a mean velocity V_0=47.6 km s^{-1}. Other reasonable choices of V_{rad} and V_0 have been tried and the results have been found not to differ strongly from those presented here. Contributions from the bubble and from the red-shifted arcs are minimized by requiring $43<V_x<52$ km s^{-1}.

While Fig. 20 gives a perfectly legitimate model of the observations, it must be clear that it may have nothing to do with reality. Indeed, such a model can be constructed for any data cube, whether expanding or not radially, a result of the under-determination of the problem. However, it provides a useful visualisation of the morphology, in particular of its topology, as long as it is interpreted with care. In particular, it is clear that it is of little value when V_x is close to V_0: in such a case, there is essentially no Doppler shift to deal with, and therefore no hope to obtain a meaningful evaluation of x from the Doppler velocity.

The north-eastern and south-eastern arms are clearly identified in the fifth and sixth panels of Fig. 20 respectively. The south-western and north-eastern outflows cover panels $(-60°<\omega<60°)$ and panels $(120°<\omega<240°)$ respectively. Detached shells are seen not only east, as expected, but also west, in the first panel. Detailed studies of the north-eastern and south-western outflows are presented in the next subsection.

In summary, the sky map of the circumbinary envelope at distances up to 2.5″ from Mira A displays some symmetry about an axis pointing ∼30° south of west but a signif-

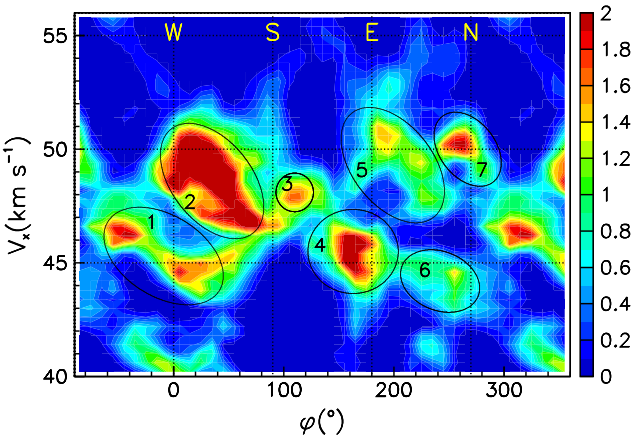

Figure 17. Position-velocity diagram in a circle centred on Mira A for distances to Mira A between 0.5″ and 2.5″. The ellipses delineate area associated with the sky maps displayed in Fig. 18.

icant dissymmetry between the associated hemispheres at distances not exceeding 1.5″: the south-western hemisphere is dominated by a broad conical outflow, referred to as the south-western outflow, while the north-eastern hemisphere is dominated by two arms, the south-eastern arm clearly related to Mira B, and the north-eastern arm. At larger distances, the two hemispheres are more similar. In particular, in both hemispheres cavities are visible, with a clearly detached shell in the north-eastern hemisphere. It looks as if at short distances a large gas volume, red-shifted and covering the north-eastern quadrant, had been swept away or prevented to emit in CO(3-2) because of temperature or turbulences or else. Obviously, in both hemispheres, winds cannot be assumed to be stationary and the observed morphology bears the marks of history. While the kinematics show clear signs of radial expansion, with typical velocities between 5 and 10 km s^{-1}, no sign of significant rotation has been detected at the level of 0.5 km s^{-1} arcsec^{-1} or more. Finally, the effective emissivity is concentrated in the vicinity of the plane of the sky rather than displaying rotational invariance about the approximate axis of symmetry observed on the sky map.

6.3 South-western and north-eastern outflows

Figure 21 shows maps of the effective emissivity in z vs ξ planes scanning across the south-western and north-eastern outflows in 10° steps in ω from −45° to 45° and 135° to 225° respectively. The south-western outflow and north-eastern arm are particularly important at $\omega = -20°$ and 160° respectively, namely back-to-back in ω. However, they both point south by some 30° and are not back-to-back in space, the north-eastern arm being the main outflow component in the northern hemisphere (one can just see part of it at $\omega = 140°$ and 150°).

In both maps, the emission is seen to be enhanced at large distances. This is spectacular in the eastern outflow where an arc covering close to a steradian contributes to all panels above ω=170°. Its contribution to the middle panel of Fig. 15, its clear separation from the bulk of the outflow and its narrow width, less than 100 AU, are reminiscent of what is observed in detached shells around some carbon stars (Maercker et al. 2014; Olofsson et al. 2010; Mattsson et al. 2007; Schöier et al. 2005). Such detached shells are usually observed on the dust rather than on the gas but there is evidence for dust and gas having similar morphologies in these cases. Also, they cover much larger solid angles, up to 4π, and are not seen in oxygen-rich M stars. The present data do not allow, without confronting them to the predictions of hydrodynamic models, to make definitive statements about the physical nature of these arcs, in particular to evaluate the respective contributions of gas density and temperature to the depression separating the arcs from the bulk. Yet, one can safely state that some violent event must have occurred some centuries ago, similar to the ejections of matter associated with thermal pulses and/or helium flashes in the case of carbon stars. In this context, the presence of a similar arc in the south-western outflow at ω=0° and possibly 10°, and of a small cavity at $\omega = -10°$, suggest a common origin for all these arcs, all distant from Mira A by some 2″, meaning 150 years or so at 7 km s^{-1}.

An interesting feature, a small apparent cavity, is seen in the north-eastern outflow at $\omega = 160°$, possibly related to Mira B which sits in the middle of the outflow for V_x=45 km s^{-1}. It is also seen in Fig. 12 between 45 and 46 km s^{-1}.

7 DISCUSSION

At distances from Mira A not exceeding 2.5″, emission is dominated by two outflows aiming respectively at ∼30° north of east and ∼30° south of west, along an axis with respect to which the sky map is approximately symmetric. However, the effective emissivity is not rotation-invariant with respect to this axis, being rather concentrated near the plane of the sky, nor is it symmetric with respect to the equator associated with this axis, defining a north-eastern and a south-western hemispheres. Moreover, we detected no rotation velocity about this axis at a level of 0.5 km s^{-1} arcsec^{-1} or more. We have tentatively identified different sources, which are listed in Table 1, together with the associated CO(3-2) flux, each region being defined by approximate intervals ΔR, $\Delta\varphi$ and ΔV_x respectively.

At distances from Mira A not exceeding ∼1.5″, the south-western emission consists of a slightly red-shifted outflow covering a broad solid angle at the scale of a steradian and expanding radially at a velocity between 5 and 10 km s^{-1}. The north-eastern emission consists instead of two slightly blue-shifted arms separated by a dark region covering the north-eastern quadrant and identified by Ramstedt et al. (2014) as a wake of Mira B. However, as Mira B is currently moving nearly north, we do not see how this dark region could be associated with its wake. Beyond ∼1.5″ and up to ∼2.5″ projected distance from Mira A, evidence has been presented for detached arcs that are reminiscent of the detached shells observed in some carbon stars and associated with thermal pulses and/or helium flashes. This is particularly spectacular in the north-eastern hemisphere, where a detached arc covers the whole quadrant,

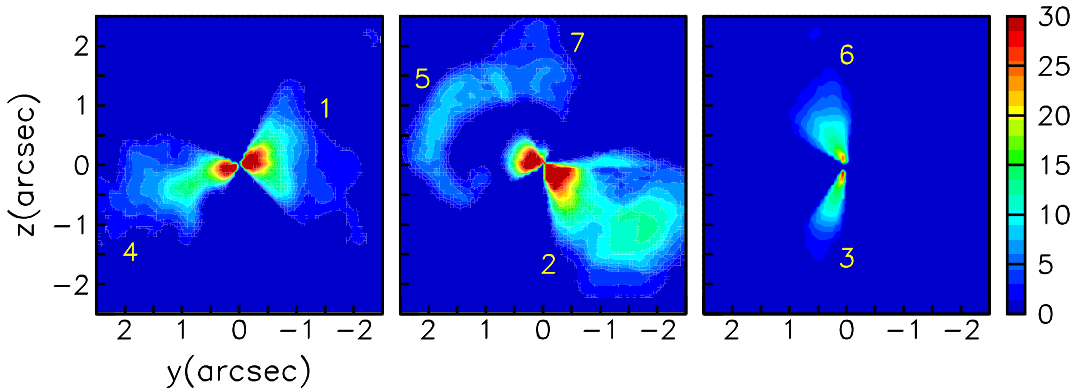

Figure 18. Maps of F (Jy km s^{-1} arcsec^{-2}) for the regions of the P-V diagram delineated by ellipses in Fig. 17.

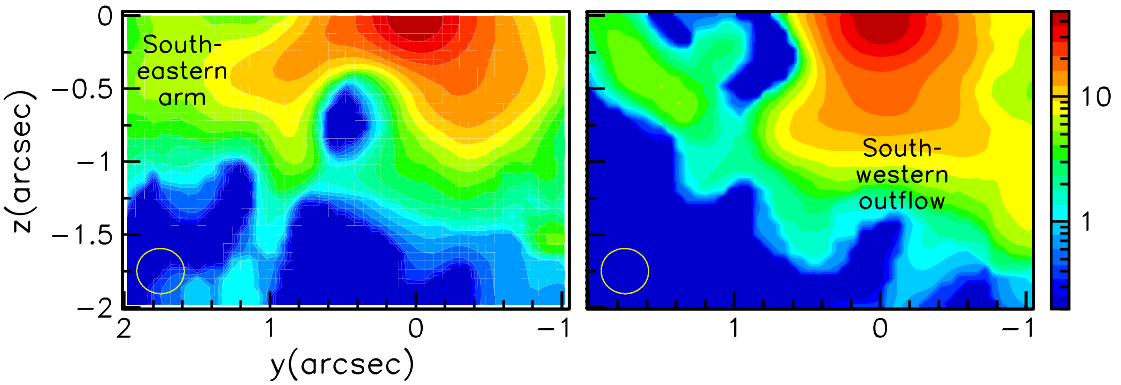

Figure 19. Sky maps of F over 43<V_x<47 km s^{-1} (left) and 47<V_x<50 km s^{-1} (right) displaying the south-eastern arm (left) and the southern limb of the south-western outflow (right). The beam is shown in the lower left corner of each panel.

Table 1. Properties of some of the main sources

Name	R ($''$)	φ ($^\circ$)	V_x (km s^{-1})	F (Jy km s^{-1})
Mira A	0-0.5	0-360	44-52	4.15
South-western outflow	0.5-2.5	−60-120	43-52	7.90
North-eastern arm	0.5-2.5	220-280	43-45.5	0.62
South-eastern arm	0.5-2.5	120-190	43-47	1.49
Eastern detached arc	1.5-2.5	180-290	47-52	1.55
Dark eastern sector	0.5-1.5	170-210 200-280	47-48.5 45.5-47	0.15

but seems also to apply, although less clearly, in the south-western hemisphere.

It is remarkable that the above description ignores the presence of Mira B. It is only when looking at the south-eastern arm in the immediate environment of the A+B pair that evidence has been found for enhanced emission from a blue-shifted gas flow having its source at Mira A and concentrated in the direction of Mira B, with a possible small contribution of gas gravitationally bound to Mira B as detected at much shorter distances by Vlemmings et al. (2015) from the continuum emission of partially ionized gas. We have shown that a gas flow emitted by Mira A and concentrating in the direction of Mira B is clearly prefered to a static gas volume surrounding Mira B. The WRLOF model of Mohamed & Podsiadlowski (2012), and in particular its Model 1 version, offers a natural framework in which to draw such a picture. It explains the enhancement around Mira B as the result of the Mira A wind leaking through the Lagrange point to Mira B, thereby implying that a large fraction of it would be channelled to Mira B and eventually be accreted onto it. This is at variance with models in which the wind escaping Mira A is isotropic, giving a chance of being trapped by Mira B to only a very small fraction of it. What is observed here favours clearly the former hypothesis over the latter but gives also evidence for two additional outflows escaping Mira A in directions far away from the

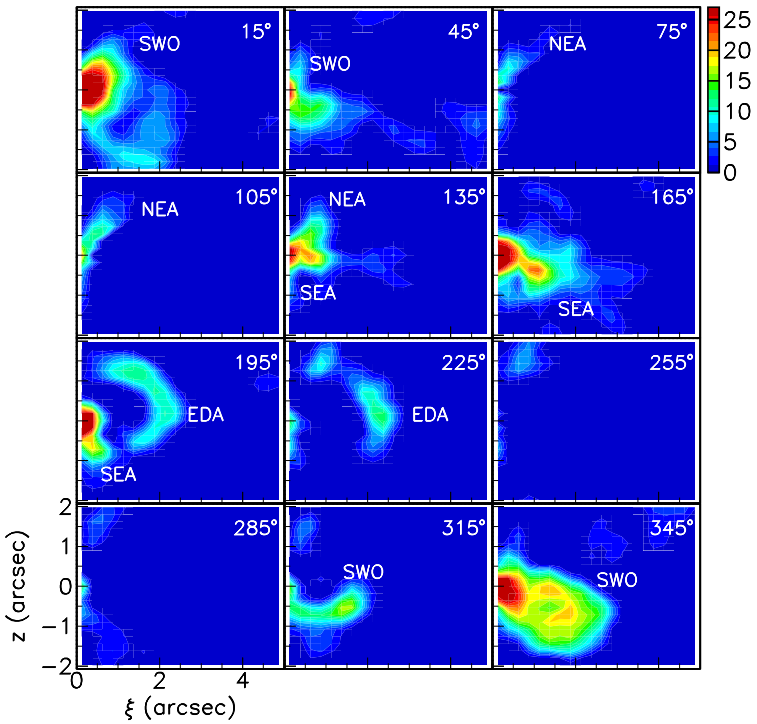

Figure 20. Maps of the effective emissivity reconstructed in space under the assumption of a pure radial expansion at constant velocity of 7 km s^{-1}. The ordinate is z and the abscissa is $\xi = \sqrt{x^2 + y^2}$. Each panel is for a 30° wide interval of ω measured clockwise from 0 on the y axis. The label in each panel gives the value of at the centre of the interval. The upper and lower rows are west, the two middle rows are east. The labels stand for south-western outflow (SWO), north-eastern arm (NEA), south-eastern arm (SEA), eastern detached arc (EDA).

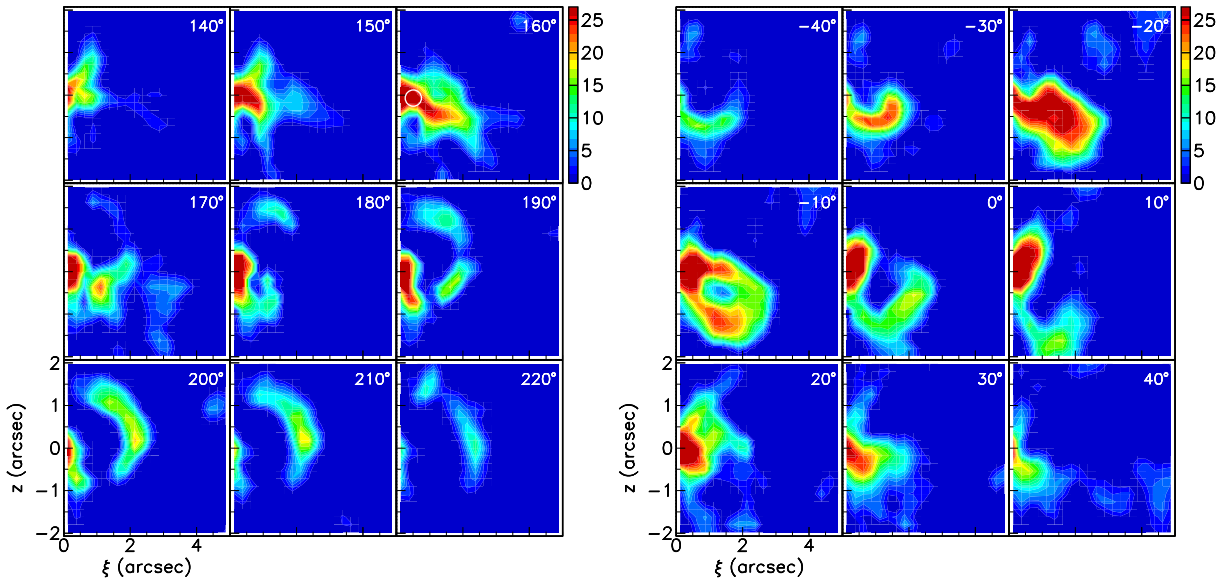

Figure 21. South-western (left) and north-eastern (right) outflows: maps of the effective emissivity reconstructed in space under the assumption of a pure radial expansion at constant velocity of 7 km s^{-1}. The ordinate is z and the abscissa is $\xi = \sqrt{x^2 + y^2}$. Each panel is for a 10° wide interval of ω measured clockwise from 0 on the y axis. The label in each panel gives the value of ω at the centre of the interval. The white circle in the $\omega = 160°$ panel shows the position of Mira B for $V_x = 45$ km s^{-1}.

Lagrange point: the north-eastern arm and the abundant south-western outflow, which are of course absent from the simple version of the WRLOF model. Assuming that the WRLOF mechanism applies, at least qualitatively, to the south-eastern arm, one would then expect a significant fraction of its flux to be accreted by Mira B and the downstream gas flux to be smaller than the upstream one. It is not clear whether the depression seen in the $\omega = 160^\circ$ panel of Fig. 21 downstream of Mira B can reliably be taken as evidence for such an effect.

The interpretation in terms of the WRLOF model was also favoured by Ramstedt et al. (2014), in particular in the context of the possible presence of spriral arcs at larger distance.

The precise role played by Mira B in shaping the circumbinary envelope raises some unanswered questions. The elongation along an approximate symmetry axis pointing 30° south of west observed in the present data is similar to that observed at 94 GHz by Vlemmings et al. (2015) who find a major axis of 0.042″, an aspect ratio of ∼1.2 and a position angle 36° south of west. However, the continuum was observed four months later than the CO line and earlier observations of the star atmosphere suggest that the position angle of the elongation is very strongly dependent on the phase of the Mira A pulsation (Karovska et al. 1991; Haniff et al. 1992; Wilson et al. 1992; Quirrenbach et al. 1992). If this were true, the similarity between the elongations observed by ALMA in the continuum and on the line would be pure coincidence. One might nevertheless still suppose that the elongation observed in the present CO data is caused by anisotropic pulsation amplitudes, which would then be responsible for shaping the outflow, causing the south-west to north-east enhancement observed here and producing the south-western outflow. In this process, dominated by the pulsation of Mira A atmosphere and its asymmetry, Mira B would play no obvious role. In the north-eastern hemisphere, however, additional mechanisms need to be invoked to explain the separation in two distinct arms. While focusing by Mira B must play a role in shaping the south-eastern arm, it is difficult to imagine how it could generate the broad dark region referred to as the dark eastern sector in Table 1. This sector suggests a deficit of some 4 Jy km s^{-1} of north-eastern emission with respect to south-western emission: how could this be related to Mira B? It seems rather related to whatever violent event produced the eastern detached arc. Of course, the emission deficit may be due to conditions of temperature preventing the population of the J=3 level of the CO molecule, the mass deficit associated with the dark eastern sector being then much smaller or even inexistent. Both the accretion disk of the white dwarf and the occurrence of thermal pulses are known to release important amounts of energy, but their relative importance in shaping the circumbinary envelope is not clear to us. To answer such questions, the present observations are but one of the factors to be taken into account, the whole multiwavelength spectrum having to be taken into consideration. In this context, observations of the emission of another molecular line of carbon monoxide would bring very useful information on the temperature distribution and allow for disentangling, at least partly, the respective roles of temperature and density.

8 SUMMARY

We have presented a description of the morphology and kinematics of the gas envelope of Mira Ceti using high spatial resolution observations of ^{12}CO(3-2) emission made by ALMA. We have tried to keep away as much as possible from preconceptions that might have biased the analysis. Yet, much is known of this source from multiwavelength observations, and this knowledge must be taken into account when trying to make sense of what has been observed. A distinctive feature of the observations analysed here is the strong imprint of the mass loss history on the morphology of the circumbinary envelope. Evidence has been presented for the distinct contributions of remnants of events that occurred a few thousand years ago and events that occurred a few hundred years ago. The former include a south-eastern blue-shifted bubble that can be described as a circular ring expanding radially at a velocity of less than 2 km s^{-1} and making an angle of ∼50° with the plane of the sky, together with a number of red-shifted arcs. The present data do not allow for a reliable association of these arcs in spirals, as proposed by Ramstedt et al. (2014) using ALMA observations having better large distance coverage.

The central region is dominated by the circumbinary envelope, displaying two outflows in the north-eastern and south-western hemispheres. At short distances from the star, up to ∼1.5″, they display very different morphologies. The south-western outflow covers a broad solid angle, expands radially at a rate between 5 and 10 km s^{-1} and is slightly red shifted. The north-eastern outflow consists of two arms, with a separation of ∼90° on the plane of the sky, both blue-shifted, bracketing a broad dark region where emission is suppressed. At larger distances from the star, between ∼1.5″ and ∼2.5″ the dissymmetry between the two hemispheres is significantly smaller and both hemispheres display evidence for detached arcs, particularly spectacular in the north-eastern hemisphere. Close to the stars, we are observing a mass of gas surrounding Mira B, with a size of a few tens of AU, and having Doppler velocities with respect to Mira B reaching 1.5 km s^{-1} in each of the red and blue directions, which we interpret as gas flowing from Mira A toward Mira B, being eventually focused or even trapped by Mira B, with a possible small contribution of gas gravitationally bound to Mira B.

Throughout the present article, emphasis has been placed on giving as simple and yet as reliable a picture of what has been observed, with the aim of helping with the conception of models that would allow for a deeper understanding of the physics at play, but the conception of such models is clearly beyond the scope of the present work.

ACKNOWLEDGEMENTS

This paper makes use of the following ALMA data: ADS/JAO.ALMA#2013.1.00047.S. ALMA is a partnership of ESO (representing its member states), NSF (USA) and NINS (Japan), together with NRC (Canada) , NSC and ASIAA (Taiwan), and KASI (Republic of Korea), in cooperation with the Republic of Chile. The Joint ALMA Observatory is operated by ESO, AUI/NRAO and NAOJ. The data are retrieved from the JVO portal

(http://jvo.nao.ac.jp/portal) operated by the NAOJ. We are indebted and very grateful to the ALMA partnership, who are making their data available to the public after a one year period of exclusive property, an initiative that means invaluable support and encouragement for Vietnamese astrophysics. We particularly acknowledge friendly and patient support from the staff of the ALMA Helpdesk. We are very grateful to Professors Anne Dutrey, Stephane Guilloteau and Thibaut Le Bertre for their interest in this work and the many helpful comments and information they have provided. Financial support is acknowledged from the Vietnam National Satellite Centre (VNSC/VAST), the NAFOSTED funding agency under contract xx, the World Laboratory, the Odon Vallet Foundation and the Rencontres du Viet Nam.

REFERENCES

Etoka S., Gérard E., Richards A., et al., 2010, Proc. of the 10th European VLBI Network Symposium and EVN Users Meeting: VLBI and the new generation of radio arrays, 6
Fong D., Meixner M., Sutton E. C., et al., 2006, ApJ, 652, 1626
Haniff C. A., Ghez A. M., et al., 1992, AJ, 103, 1662
Ireland M. J., Monnier J. D., et al., 2007, ApJ, 662, 651
Josselin E., Mauron N., Planesas P. & Bachiller R., 2000, A&A, 362, 255
Karovska M., Hack W., et al., 1997, ApJ, 482, L175
Karovska M., Schlegel E., Hack W., et al., 2005, ApJ, 623, L137
Karovska M., Nisenson P., Papaliolios C. & Boyle R. P., 1991, ApJ, 374, L51
Kipper T., 1992, Baltic Astronomy, 1, 190
Knapp G. R., Young K., et al., 1998, ApJS, 117, 209
Little S. J., Little-Marenin I. R. & Bauer W. H., 1987, AJ, 94, 981
Maercker M., Ramstedt S., Leal-Ferreira M. M. L., et al., 2014, A&A, 570, A101
Marengo M., Karovska M., et al., 2001, ApJ, 556, L47
Martin D. C., Seibert M., Neil J.D., et al., 2007, Nature, 448, 780
Matthews L. D. & Karovska M., 2006, ApJ, 637, L49
Matthews L. D., Libert Y., Gérard E., et al., 2008, ApJ, 684, 603
Matthews L. D., Reid M. J. & Menten K. M., 2015, ApJ, 808, 36
Mattsson L., Höfner S. & Herwig F., 2007, A&A, 470, 339
Mauron N. & Caux E., 1992, A&A, 265, 711
Mayer A., Jorissen A., et al., 2011, A&A, 531, L4
Meaburn J., López J. A., Boumis P., et al., 2009, A&A, 500, 827
Mohamed S. & Podsiadlowski P., 2012, BaltA, 21, 88 and references therein
Olofsson H., Maercker M., et al., 2010, A&A, 515, A27
Planesas P., Bachiller R., Martin-Pintado J. & Bujarrabal V., 1990, ApJ, 351, 263
Planesas P., Alcolea, J. & Bachiller R., 2016, A&A, 586, A69
Prieur J. L., Aristidi E., Lopez B., et al., 2002, ApJS, 139, 249
Quirrenbach A., Mozurkewich D., Armstrong J. T., et al., 1992, A&A, 259, L19
Ramstedt S., Mohamed S., Vlemmings W. H. T., et al., 2014, A&A, 570, L14
Ryde N. & Schöier F. L., 2001, ApJ, 547, 384
Schöier F. L., Lindqvist M. & Olofsson H., 2005, A&A, 436, 633
Sokoloski J. L. & Bildsten L., 2010, ApJ, 723, 1188
Templeton M. R. & Karovska M., 2009, ApJ, 691, 1470
Turon C., Creze M., Egret D., et al., 1993, Bull. Inf. Cent. Donnees Astron. Strasbourg, 43, 5
Ueta T., 2008, ApJ, 687, L33
van Leeuwen F., 2007, A&A, 474, 653
Vlemmings W. H. T., Ramstedt S., O'Gorman E., et al., 2015, A&A, 577, L4
Wilson R. W., Baldwin J. E., Buscher D. F. & Warner P. J., 1992, MNRAS, 257, 369
Wood B. E., Karovska M. & Raymond J. C., 2002, ApJ, 575, 1057
Woodruff H. C., Eberhardt M., et al., 2004, A&A, 421, 703
Wyatt S. P. & Cahn J. H., 1983, ApJ, 275, 225

APPENDIX A:

This paper has been typeset from a TEX/LATEX file prepared by the author.

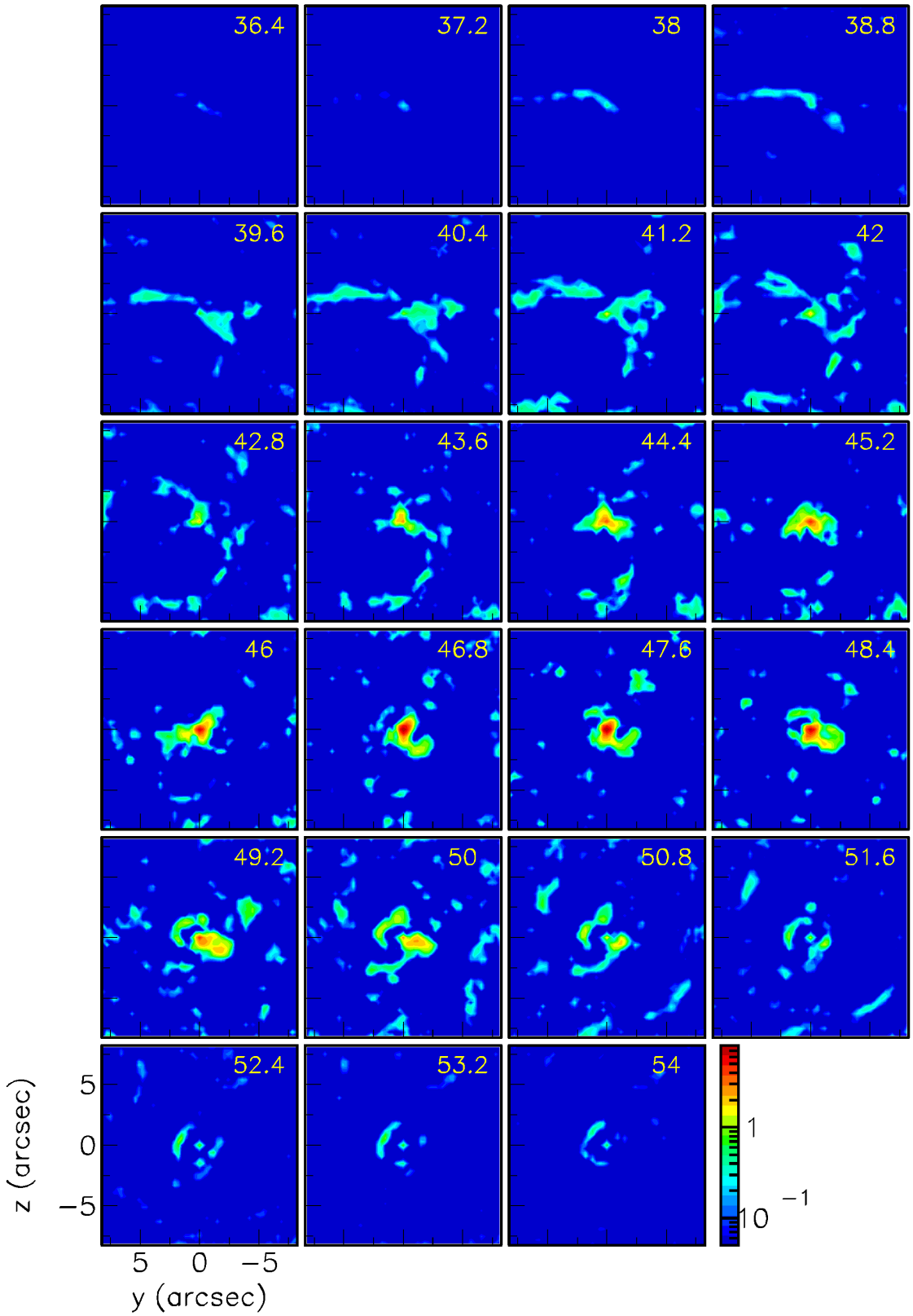

Figure A1. Channel maps covering $8.2'' \times 8.2''$ obtained by grouping two adjacent velocity channels (resulting in a width of 0.8 km s^{-1}) between 36.0 and 54.4 km s^{-1}. Each panel is labelled with the central velocity (km s^{-1}). The colour scale is in units of Jy km s^{-1} arcsec^{-2}.